LM-04K144
November 16, 2004

# Zinc Treatment Effects on Corrosion Behavior of Alloy 600 in High Temperature, Hydrogenated Water

SE Ziemniak and ME Hanson

# Zinc Treatment Effects on Corrosion Behavior of Alloy 600 in High Temperature, Hydrogenated Water

Stephen E. Ziemniak
Michael Hanson

September 2004

Lockheed Martin Corporation
P. O. Box 1072
Schenectady, New York, 12301-1072

ABSTRACT

Trace levels of soluble zinc(II) ions (30 ppb) maintained in mildly alkaline, hydrogenated water at 260°C were found to reduce the corrosion rate of Alloy 600 (UNS N06600) by about 40% relative to a non-zinc baseline test [2]. Characterizations of the corrosion oxide layer via SEM/TEM and grazing incidence X-ray diffraction confirmed the presence of a chromite-rich oxide phase and recrystallized nickel. The oxide crystals had an approximate surface density of 3500 $Fm^{-2}$ and an average size of 11 ± 5 nm. Application of X-ray photoelectron spectroscopy with argon ion milling, followed by target factor analyses, permitted speciated composition vs. depth profiles to be obtained. Numerical integration of the profiles revealed that: (1) alloy oxidation occurred non-selectively and (2) zinc(II) ions were incorporated into the chromite-rich spinel: $(Zn_{0.55}Ni_{0.3}Fe_{0.15})(Fe_{0.25}Cr_{0.75})_2O_4$. Spinel stoichiometry places the trivalent ion composition in the single phase oxide region, consistent with the absence of the usual outer, ferrite-rich solvus layer. By comparison with compositions of the chromite-rich spinel obtained in the non-zinc baseline test, it is hypothesized that zinc(II) ion incorporation was controlled by the equilibrium for

$$0.55\ Zn^{2+}(aq) + (Ni_{0.7}Fe_{0.3})(Fe_{0.3}Cr_{0.7})_2O_4(s) \quad W$$

$$0.40\ Ni^{2+}(aq) + 0.15\ Fe^{2+}(aq) + (Zn_{0.55}Ni_{0.3}Fe_{0.15})(Fe_{0.3}Cr_{0.7})_2O_4(s)$$

It is estimated that only 8% of the Ni(II) ions generated during non-selective oxidation of the alloy were retained as Ni(II) in the corrosion layer; the remainder either recrystallized to Ni(0) (38%) or were released to the aqueous phase (54%).

KEYWORDS: (A) Superalloys; (B) AES, XPS, X-ray diffraction; (C) oxidation, passive films

## INTRODUCTION

The application of nickel-base CrFe alloys in hydrothermal environments, where dissolved hydrogen is also present, results in extremely low corrosion rates. Two reasons are responsible for such behavior: (1) nickel-base alloys are inherently more resistant to oxidation than iron-base alloys and (2) the redox environment favors stability of nickel metal relative to nickel(II) oxide. For example, a change in NiCrFe composition from an iron-based 18Cr8Ni alloy (UNS S30400) to a nickel-based 16Cr9Fe alloy (UNS N06600) lowers the parabolic rate constant by a factor of 20 [1, 2].

Duplex corrosion oxides form on these materials as a result of non-selective oxidation and immiscibility in the appropriate spinel binary: $Ni(Fe_{1-x}Cr_x)_2O_4$, x . 0.15, 0.7 for nickel-base alloys and $Fe(Fe_{1-x}Cr_x)_2O_4$, x . 0.05, 0.7 for iron-base alloys. The inner, chromite-rich, solvus layer is believed to provide a protective barrier to retard additional corrosion. On the other hand, corrosion studies of Alloy 600 have shown that growth of the outer, ferrite-rich, solvus layer is enhanced by pickup of dissolved iron ions from the aqueous phase. By co-precipitating with the (excess) nickel(II) ions created by non-selective oxidation, recrystallization as nickel metal is lessened.

Other divalent metal ions, compatible with the spinel oxide lattice, may be added to the aqueous phase to further modify the oxide corrosion layer and influence the corrosion behavior of NiCrFe alloys. The pickup of radioactive cobalt by ex-reactor FeCrNi alloy surfaces in light water nuclear reactor coolant systems is a well-known example of the former, while zinc coolant treatment lessens this phenomenon. Pickup of zinc(II) ions by an iron-base CrFe alloy has been shown to: (1) alter the divalent ion composition of the ferrite-rich solvus, (2) reduce its quantity/crystal size, (3) create recrystallized nickel in the oxide layer, (4) alter the divalent ion

composition of the chromite-rich solvus and (5) lower the corrosion rate. Maintenance of 30 ppb zinc ion levels caused 20 mol % of the divalent cations in the chromite-rich solvus to be replaced by Zn(II) and lowered the corrosion rate of austenitic stainless steel by about a factor of 5 relative to a non-zinc baseline test after 10,000 hr at 260°C [3].

The present investigation was undertaken to determine the manner in which similar trace levels of soluble zinc affect the corrosion behavior of a nickel-base CrFe alloy whose Cr/Fe ratio approximates that of the chromite-rich solvus.

## EXPERIMENTAL

Corrosion specimens of NiCrFe Alloy 600 (UNS N06600) were exposed at 260°C in a flowing autoclave facility (10 $cm^3$/min) comprised of a one liter, type 347 stainless steel (UNS S34700) vessel, and fed from stainless steel tanks containing deionized, hydrogen-sparged water. The dissolved hydrogen concentration was 45 $scm^3$/kg water; alkalinity was buffered to maintain pH (@260°C) = 6.70. A packed bed of granular zinc(II) oxide, located upstream of the test autoclave, was used to supply constant, trace levels of soluble zinc(II) ions. Target zinc concentrations (~30 ppb) were achieved by controlling the feedwater temperature, since the solubility behavior of ZnO had been previously determined as a function of temperature [4]. Test shutdowns, along with specimen removals and insertions, occurred intermittently, so that exposure times ranged between 1000 and 10,000 hours.

In anticipation of the precision corrosion film analyses to be performed, one side of each corrosion specimen (5/80 x 3/40 x 1/160) was highly polished (<6 Fin AA) using diamond grit paste. Larger, machined coupons (40 x 3/40 x .0320) were also prepared and exposed along with the polished specimens. The larger surface area of the former permitted the total quantity

of oxidized base metal to be accurately determined via the application of standard chemical descale (i.e., gravimetric) methodology.

## ANALYTICAL PROCEDURES

After completion of the test exposure period, the corrosion coupons were chemically descaled and the smaller corrosion specimens were subjected to three types of analyses to characterize the states of their oxidized surfaces: (1) scanning (SEM) and transmission (TEM) electron microscopy with X-ray spectroscopy (EDX), (2) grazing incidence X-ray diffraction (XRD) and (3) X-ray photoelectron spectroscopy (XPS). Details of each of these methodologies were provided previously [1, 2]. It is noted that application of argon ion milling together with target factor analysis allowed XPS to obtain depth profiles for elements and their oxidation states. Corrections for sputter damage were also included in the TFA.

Due to the nearly non-visible changes in appearance of all specimens during testing, it was necessary to adapt the above analytical procedures to ensure adequate resolution of relatively small oxide crystals and thin corrosion films. For example, the SEM analyses were performed with an FEI Company Sirion model instrument, equipped with a Schottkey field emission electron source, which provided magnifications up to 150,000X. The XRD analyses were performed using synchrotron radiation, rather than conventional X-ray sources, to permit determination of oxide film thicknesses on the order of a few hundred Angstroms. In this manner, a critical penetration depth around 14 nm was attained for an angle of grazing incidence between 0.2 and 0.3°.

## RESULTS

### A. Gravimetric Analysis

The AP/AC method was very effective in removing the corrosion oxide layer while minimizing attack of the alloy substrate. Specimen descale weight losses due to corrosion (corrected for base metal attack during scale removal) are summarized in Table I. These data were converted to surface densities by dividing by the surface area per specimen (0.4078 $dm^2$) and correlated to an expected parabolic rate expression:

$$w,\ mg\ (alloy)\ dm^{-2} = (K_p)\ t^{1/2}$$

The parabolic rate constant ($K_p$) was found to be $0.033 \pm 0.014$ mg $dm^{-2}$ $hr^{-1/2}$.

The gravimetric analyses also recorded specimen weight changes during testing, which may be caused by: (1) pickup and retention of oxygen from the corrosion process as well as zinc and iron ions from the coolant, (2) release of solubilized nickel ions to the aqueous phase and (3) sloughage of corrosion oxide crystals. Due to the adherent nature of the corrosion oxide crystals, it is expected that sloughage will be insignificant and the weight change during corrosion will be defined by the difference between pickup/retention of oxygen, zinc and iron ions from the aqueous phase and the dissolution/release of nickel ions to the aqueous phase.

As shown in Table I, the weights of all corrosion specimens decreased during testing. To provide a rational basis for analyzing these decreases, estimates are provided for oxygen pickup based on the amounts of oxygen required to form corrosion oxide spinels - $Ni(Fe,Cr)_2O_4$. For example, in the case of zero release

final wgt. = pretest wgt. + oxygen in corr. oxide

If it is assumed that the zero release case is represented by the complete retention of recrystallized nickel and all spinels, then a material balance reveals that 4.3 moles of Ni will be formed for each mole of spinel created, i.e., corrosion layer is 47.6 wgt.% spinel. Since the

overall spinel composition, $Ni(Fe_{0.34}Cr_{0.66})_2O_4$, has an oxygen content of 27.9 wgt.%, the weight change for zero release is written

$$\text{zero release} = \text{wgt. gain due to oxygen in corr. oxide} = \frac{(0.476)(0.279)}{(1-0.279)}\ x\ (\text{metals oxidized})$$

On the other hand, specimen weight losses were bounded by complete loss of all oxidized metals. Therefore, by expressing specimen weight change as a fraction of the maximum weight change between the zero and complete release limiting cases, the fraction of corroded alloy released to the aqueous phase was determined.

The above corrosion release calculations, as summarized in Table I, indicate that significant amounts of corrosion release occurred: excluding the shortest exposure results as inaccurate, the test average is 41 ± 4%. This result probably underestimates the true value, since the small amounts of zinc pickup have been neglected.

B. Scanning and Transmission Electron Microscopy

Visual appearances of all specimens upon removal from testing remained shiny and remarkably unchanged by exposure to the test environment. Views of the corroded specimen surfaces, recorded by high magnification SEM photographs (shown in Fig. 1), reveal complete coverage by a layer of extremely fine crystals. Application of digital imaging software to the SEM photographs revealed that the number density (~3500 $Fm^{-2}$) and size distribution (11 ± 5 nm) of the oxide crystals were relatively unaffected by exposure time, see Fig. 2. Approximating the oxide layer by spheres having a density of 5.2 gm $cm^{-3}$, and integrating the given size distributions, provides the weight of a monolayer for the three exposures as: 0.22, 0.26 and 0.34 mg $dm^{-2}$. Combining these (oxide) estimates with the expected amounts of spinel oxide created

during corrosion (i.e., 0.476 x Table I value) allows the amounts of corrosion to be restated in monolayer thicknesses: 2, 6 and 6 for exposures of 1000, 5000 and 10,000 hours, respectively.

Microchemical analyses of the oxide crystals were performed on a 10,000 hr specimen by applying transmission electron microscopy. A planar view through the surface corrosion oxide is shown in Fig. 3. Consistent with Figs. 1 and 2, the crystals are seen to range in size between 5 and 30 nm. The presence of a cubic crystalline lattice, typical of spinel oxides ($a_o$ . 0.84 nm), is indicated by the electron diffraction pattern superimposed in the figure.

EDX spectra obtained from the crystals indicate the presence of oxygen and chromium (major) with lesser amounts of nickel, iron and zinc. Upon normalizing the metal ion content to 100% and applying stoichiometric constraints implied by a spinel ($AB_2O_4$), the sum of Ni(II) and Zn(II) (~33%) indicates that no Fe(II) ions are present; the Cr(III) ion content (~42%) completes the spinel identification as $(Ni_yZn_{1-y})(Fe_{0.35}Cr_{0.65})_2O_4$, where y . 0.7. These results are consistent with the absence of Fm-sized, ferrite-rich, outer-layer crystals in the SEM photographs.

C. Grazing Incidence X-ray Diffraction

A full scan GIXRD pattern for a 10,000 hr corrosion specimen is shown in Fig. 4 for an incident angle **N** = 0.5°. Superimposed on the figure are spectra expected for magnetite, a typical spinel, and metallic nickel. Three crystalline phases are evident: (1) a spinel phase (i.e., the corrosion oxide), (2) a nickel phase (i.e., unoxidized Alloy 600 substrate) and (3) a secondary nickel phase. The second nickel phase appears as high-angle shoulders on the peaks of the Alloy 600 substrate. Its refined lattice parameter (see Table II) is nearly coincident with that of pure nickel ($a_o$ = 3.542 D per PDF Card 4-850), thus confirming the presence of recrystallized nickel in the corrosion oxide.

Using methodology developed previously [2], accurate unit cell dimensions for the crystalline solids were obtained by refining the raw data in two stages: (1) applying a prepositioning procedure, in which observed peak positions (2**2**$_{obs}$) and FWHM were determined by fitting the Pearson VII function to each peak profile, followed by (2) correcting for changes in the index of refraction. The latter effect causes all diffraction peaks to be shifted to slightly higher angles than those calculated from Bragg's law. For **N**<0.01 rad, the shift in 2**2** is given by

$$\Delta 2\theta = 2\theta_{obs} - 2\theta_{cor} = \frac{2\delta}{\sin(2\theta_{cor})} + \frac{\delta}{\phi}$$

where **)** 2**2** and **N** are given in radians. The results of these calculations for **N** = 0.5° are given in Table II. Unit cell parameters were finally determined from the corrected peak positions by least-squares refinement.

The lattice parameter calculated for the major nickel phase is identical to that for Alloy 600 ($a_o$ = 3.561(1) D), determined for an unexposed specimen in the same manner. On the other hand, the extremely thin corrosion layer produced weak reflections, which resulted in a relatively imprecise lattice parameter determination: $a_o$ = 8.377(3) D. A lattice parameter estimate for the $Zn(Fe_{0.35}Cr_{0.65})_2O_4$ binary, assuming a linear increase between $ZnCr_2O_4$ ($a_o$ = 8.328 D) and $ZnFe_2O_4$ ($a_o$ = 8.441 D), provides $a_o$ = 8.368 D. Therefore, the lattice parameter of the corrosion oxide spinel is consistent with a zinc-rich, mixed chromite/ferrite spinel.

It is noteworthy that all XRD peaks in Fig. 4 are broader than expected for bulk phases. As discussed previously [2], broadening of the Alloy 600 substrate peaks is attributed to surface microstrain created during specimen fabrication/mechanical polishing (and is confined to the

surface region), while broadening of the spinel peaks is attributed to the small size of the oxide crystals. In the first case, the ratio FWHM/tan **2** is independent of **2** and in the second case the product FWHM cos **2** is independent of **2**. An estimate of grain size was obtained by applying the Scherrer equation [5] using full width at half maximum (FWHM) of the [311] spinel peak:

$$size \approx \frac{0.94\,\lambda}{FWHM \cdot \cos\theta}$$

where **8** = 1.15 D and **2** = 13°. In this manner, the size of the spinel crystals was determined to be 7.6 nm (FWHM = 0.84°). This calculation probably underestimates the true crystal size because the instrumental contribution is neglected. Therefore, the XRD crystal size estimates agree with those observed by SEM.

Rough estimates of the oxide layer thickness were obtained by monitoring: (1) the emergence of the Ni [111] peak and (2) the changes in intensity of the spinel [311] peak, at increasing angles of grazing incidence. As shown in Fig. 5, 'breakout' of the Ni [111] substrate peak at 2**2** . 32.5° had already occurred at the lowest angle of grazing incidence (**N** = 0.1°). Assuming a uniform coverage and applying the penetration depth formula for **N** = 0.1°, we estimate the oxide thickness to be . 2.5 nm. Similarly, increases in **N** between 0.2 and 0.5° had virtually no impact on intensity of the spinel [311] peak, indicating that spinel thickness was <4 nm.

D. X-Ray Photoelectron Spectroscopy

Surface atom densities were extracted from the integrated, pre-processed XPS data using MultiPack software in a manner described previously. As expected, the major elements quantified were oxygen, nickel, chromium, iron and zinc. Significant levels of carbon were also detected on the unsputtered surfaces of all specimens. The initial sputtering operation reduced the carbon signals to negligible levels, indistinguishable from that of the base alloy composition.

This behavior is consistent with that expected for an adsorbed layer of hydrocarbon contamination (i.e., organic carbon) [6]. Therefore, carbon was excluded when the surface atom densities were normalized to 100% to obtain units of atom percent.

Oxygen levels in the unsputtered surface were always greater than could be accounted for from the quantity of oxidized metals, implying that an additional constituent was present. Subsequent refinement of the O(1s) region by TFA revealed the presence of a second eigen-spectrum around 532.2 eV, which corresponds to $O^{2-}$ in adsorbed water [7]. This peak was not present after sputtering.

Elemental composition versus depth profiles obtained in the above manner are shown in Fig. 6 for typical test specimens. Two features of these profiles are noteworthy: (1) existence of elongated oxygen 'tails' and (2) approach to Alloy 600 composition by nickel, chromium and iron as oxygen goes to zero. The oxygen tails appear to be a manifestation of the non-uniform, polycrystalline nature of the oxide layer. Consistent with our previous analyses [1, 2], oxide thicknesses were determined by the first derivative method, i.e., where the slope of each oxygen profile reached a maximum with respect to depth and the second derivative became zero. This condition represents the depth at which sputter removal of the oxide layer exposes the alloy substrate most rapidly.

Inferred thicknesses of the corrosion oxide layer, based on the oxygen profiles shown in Fig. 7, are given in Table III. For consistency with the corrosion kinetics described previously, where increases in oxide thickness were correlated with a parabolic growth rate expression, we take

$$\text{O(1s) depth, } D = (K_{po})t^{1/2}$$

Excluding the outlier at 1000 hr, a least-squares fit gives $K_{po} = 2.91 \pm 0.51$ D $hr^{-1/2}$. Converting to weight of metal oxide, assuming an oxide density . 5.1 g $cm^{-3}$, gives $K_{po} = 0.015$ mg (spinel) $dm^{-2}$ $hr^{-1/2}$. Assuming non-selective oxidation and recrystallization of all excess nickel(II) as Ni, allows the oxide formation constant to be converted to $K_p = 0.032$ mg (alloy) $dm^{-2}$ $hr^{-1/2}$, a value in excellent agreement with the gravimetric result. It is noted that the conversion also assumes that contributions from corrosion release and zinc pickup are negligible (or offsetting).

Table III also includes compositions of the Alloy 600 substrate determined from XPS recorded for Ni(2p), Cr(2p) and Fe(3p) at large sputter depths where O(1s) 0. The results compare well with the (known) chemical composition of NiCrFe Alloy 600 and serve as a self-consistency check on the accuracy of the experimental methodology.

Applying our previously-developed methodology [1, 2], three eigen-spectra were fitted to three of the four XPS regions using target factor analysis (TFA). The oxidation states quantified in this manner include: Ni(II), Ni(0), Cr(III), Cr(0), Fe(II,III) and Fe(0); all sputter-damaged components being added to the oxidized metal ion inventory. Only one eigen-spectrum was fitted in the Zn(2p) region, i.e., Zn(II). By simultaneously fitting the eigen-spectra and their relative amounts as a function of depth, the XPS for each elemental constituent in the corrosion layer was quantitatively deconvoluted.

A speciated composition profile for the 10,000 hr Alloy 600 corrosion specimen, whose elemental composition profile was shown in Fig. 6, is illustrated in Fig. 8. To facilitate oxide comparisons, two profile types are shown: (a) a cross-hatched/solid split between oxidized metal and unoxidized metal, and (b) the indicated stoichiometry of the spinel oxide $(Ni_yZn_zFe_{1-y-z})(Fe_{2-x}Cr_x)O_4$. Table IV summarizes the total amount and overall stoichioimetry of the corrosion layer determined by numerically integrating each composition profile with respect to depth.

Although TFA could not distinguish between metallic nickel in unoxidized Alloy 600 and the recrystallized nickel phase found by GIXRD, the split between these two states was determined indirectly by employing the TFA results for chromium. That is, the expected amounts of unoxidized nickel from Alloy 600 were estimated from the amounts of unoxidized chromium found by TFA. Since the total amounts of metallic nickel found by TFA were always greater than those calculated above, the amounts of recrystallized nickel was determined by difference between the two:

$$\text{Recrys. } Ni = Ni(TFA) - Cr(TFA)\left(\frac{Ni}{Cr}\right)_{alloy}$$

To allow for a slight bias in the XPS results noted in Table III, the Ni/Cr ratio used for Alloy 600 was taken from the Table III results, rather than its known, actual composition. The results of these analyses are summarized in the final column of Table IV. Conversion to mg $dm^{-2}$ was accomplished by multiplying the integrals by densities of 5.1 g $cm^{-3}$ and 8. 51 g $cm^{-3}$ for the respective oxide and metal phases.

The integrals show that: (1) zinc(II) ions dominate the divalent metal ion constituents in the spinel oxide, (2) the calculated overall spinel stoichiometry is $(Zn_zNi_yFe_{1-z-y})(Fe_{1-x}Cr_x)_2O_4$, where z = 0.55, y . 0.30 and x . 0.75, and (3) the elemental composition of the metallic phase closest to the corrosion oxide layer is enriched in nickel relative to the composition of Alloy 600. Although concentration gradients consistent with the inward diffusion of Zn(II) and outward diffusion of Fe(II) are evident, reporting an average composition appears to be a legitimate approximation. Furthermore, the indicated average chromite content of the spinel (x . 0.75) represents a level high enough to place it in the single phase region of the nickel chromite-nickel ferrite binary.

## DISCUSSION

### A. Corrosion Kinetics

The combination of a low corrosion rate with limitations in the chemical descale process led to a relatively imprecise determination of the parabolic rate constant: 0.033±0.017 mg (alloy) $dm^{-2}$ $hr^{-1/2}$. This result, however, was shown to be consistent with that determined from analysis of oxygen profiles on the corroded surfaces by XPS. The calculated $K_p$ value represents a 40% reduction compared to $K_p = 0.055 \pm 0.009$ mg alloy $dm^{-2}$ $hr^{-1/2}$ determined in the absence of zinc treatment [2], see Fig. 9. It is noteworthy that a similar 40% reduction in Alloy 600 corrosion rate was obtained previously by Esposito et al. [8] for 50 ppb Zn(II) ion additions to hydrogenated water at 330°C.

### B. Characteristics of Corrosion Film

The corrosion of NiCrFe Alloy 600 in a mildly alkaline, hydrothermal environment containing dissolved hydrogen and trace levels of soluble zinc(II) ions, leads to the formation of a chromite-rich spinel oxide that contains significant amounts of recrystallized nickel. Significant amounts of divalent zinc ions are also incorporated into the spinel oxide. The atom ratio of trivalent ions in the spinel (Cr/Fe = 2.3) is approximately the same as that in the parent alloy (Cr/Fe . 1.9). This composition also coincides with that of the chromite-rich solvus phase expected in the nickel chromite-nickel ferrite spinel binary.

Based on the estimated weight of an oxide monolayer, obtained by applying digital imaging software to high resolution FEG-SEM photographs of the corroded surfaces, i.e., 0.34 mg oxide $dm^{-2}$ at 10,000 hr, it is concluded that the corrosion 'film' is composed of multiple layers of extremely fine crystals. When combined with metal ion estimates found by descale analysis (Table I) or XPS (Table IV), the 10,000 hr results indicate the presence of 6 or 4 monolayers,

respectively. Due to the good agreement between these two independent methods, the GIXRD oxide thickness result (based on Ni breakthrough) appears to be biased by the presence of recrystallized nickel.

Material balances for oxidized chromium and iron were performed using results from the integrated XPS composition vs. depth profiles and the parabolic corrosion kinetics assuming non-selective oxidation, see Table V. All of the oxidized chromium and iron are accounted for; i.e., the material balances close to within 0.2 mg $dm^{-2}$ for both alloying constituents, implying that all of the oxidized chromium and iron ions are retained in the oxide corrosion layer.

Closure of the iron material balance assuming complete retention of non-selectively oxidized iron from the alloy is noteworthy because it represents a departure relative to the results for non-zinc chemistry. As reported in Ref. [2], non-zinc chemistry resulted in pickup of iron cations from the aqueous phase, which recrystallized hydrothermally with outwardly diffusing Ni(II) ions. It is likely that such behavior is not observed in zinc chemistry because the in situ recrystallization of Ni(II) to elemental nickel is promoted, as confirmed by GIXRD. It is also possible that the lack of a ferrite layer could be due to less iron in solution when a test is run with zinc in solution. That is, zinc-induced modifications to the corrosion film on the (stainless steel) autoclave system surfaces results in a lower solubility/corrosion release of iron to the test water.

The material balance for nickel is more complex because significant quantities of the oxidized nickel underwent recrystallization back to the metallic state or were selectively released into the aqueous phase. By subtracting the amounts of Ni(II) and recrystallized Ni(0) found in the corrosion layer by XPS from the amounts of Ni(II) generated by non-selective oxidation of Alloy 600, a loss (i.e., corrosion release) rate of Ni(II) to the aqueous phase was determined. The

average value shown in Table V (54 ± 5%) is slightly greater than the coarse estimates shown in Table I (41 ± 4%) based on weight losses during testing.

It is noteworthy that the small difference in corrosion release estimates based on the XPS vs. the gravimetric analyses is consistent with neglect of zinc pickup in the gravimetric analysis. Since corrosion specimen weight changes actually represent the difference between (nickel) release and (zinc) pickup, the Table I weight losses were increased by the amounts of zinc pickup determined by XPS in Table IV. In this manner, refined gravimetric estimates of corrosion release are increased by about 6%, which allows closure of the material balances for zinc as well as nickel.

Thus, zinc pickup is believed to prevent iron pickup, so the outer, ferrite-rich solvus layer, which forms when zinc is absent, cannot form. Because the excess quantities of divalent nickel ions, created during non-selective oxidation, are not stabilized as nickel ferrite, they recrystallize and are retained in the corrosion layer. Therefore, the quantitative presence of recrystallized nickel and the absence of an outer, ferrite-rich solvus phase can be explained.

C. Inferred Zinc Equilibrium

The two most-noticeable changes in the corrosion behavior of Alloy 600 caused by zinc treatment are: (1) a lower corrosion rate and (2) elimination of the outer ferrite-rich solvus by facilitation of Ni(II) ion recrystallization to Ni. The two changes are apparently due to chemical modification of the rate-controlling, chromite-rich (solvus) phase. By comparing stoichiometries with those found in the absence of zinc treatment [2], it is seen that both Ni(II) and Fe(II) ions are being replaced in tetrahedral sites of the spinel lattice by Zn(II) ions:

$$(Ni_{0.7}Fe_{0.3})(Fe_{0.3}Cr_{0.7})_2O_4(s) + 0.55\ Zn^{2+}(aq) \rightleftharpoons (Zn_{0.55}Ni_{0.3}Fe_{0.15})(Fe_{0.3}Cr_{0.7})_2O_4(s) + 0.40\ Ni^{2+}(aq) + 0.15\ Fe^{2+}(aq)$$

The equilibrium constant for the above substitution reaction is written

$$K_{eq} = \frac{\left[Ni^{2+}(aq)\right]^{0.40}\left[Fe^{2+}(aq)\right]^{0.15}}{\left[Zn^{2+}(aq)\right]^{0.55}}$$

Soluble levels of Zn(II), Fe(II) and Ni(II) in the present test were determined by ICP-MS to be 30, 1.5 and 0.6 ppb, respectively. Based on the known hydrolytic behavior of these ions [4], it was determined that $[Zn^{2+}(aq)]/[Zn_{tot}] = 0.00033$, $[Fe^{2+}(aq)]/[Fe_{tot}] = 0.026$ and $[Ni^{2+}(aq)]/[Ni_{tot}] = 0.468$, which allowed the above equilibrium constant to be determined as $K_{eq} = 4.68$. Although $\Delta G°$ may now be obtained for the substitution reaction from $K_{eq}$, closure is not yet possible, because free energy estimates for the two chromite-rich spinels are unavailable and beyond the scope of this paper, cf. [9]. However, by comparison with the results from zinc testing with 304 stainless steel, where divalent ions in the chromite-rich solvus had higher Fe(II) ion levels, it is seen that Zn(II) replaces Ni(II) more readily than Fe(II):

$$0.2\ Zn^{2+}(aq) + Fe(Fe_{0.35}Cr_{0.65})_2O_4(s) \rightleftharpoons 0.2\ Fe^{2+}(aq) + (Zn_{0.2}Fe_{0.8})(Fe_{0.35}Cr_{0.65})_2O_4(s)$$

A trend toward higher Zn(II) levels is expected because the available sites are tetrahedral and $Ni^{2+}$ is much less compatible with tetrahedral sites than $Fe^{2+}$ [10].

ACKNOWLEDGEMENT

The professional assistance of the following individuals contributed to the successful execution of the experimental program: R. R. Shaulis, for test operation; G. M. Neugebauer, for high resolution SEM; N. Lewis, for TEM/EDX analyses; Y. Gao (GE Corporate R&D Center), for GIXRD; B. A. Tatanus, for chemical descale analyses; and D. P. Buono, for digital imaging analyses.

## REFERENCES


1. S. E. Ziemniak and M. Hanson, Corros. Sci. 44, 2209 (2002)
2. S. E. Ziemniak and M. Hanson, (Encl. 1)
3. S. E. Ziemniak and M. Hanson, manuscript submitted to Corros. Sci.
4. S. E. Ziemniak, PPChem. 3, 193 (2001)
5. R. Jenkins and R. L. Snyder, Introduction to X-Ray Powder Diffraction, John Wiley & Sons, New York, 1996
6. E. DeVito, P. Marcus, Surf. Interface Anal. 19, 403 (1992)
7. W. P. Yang, D. Costa, P. Marcus, J. Electrochem. Soc. 141, 111 (1994)
8. J. N. Esposito, G. Economy, W. A. Byers, J. B. Esposito, F. W. Pement, R. J. Jacko and C. A. Bergmann, Fifth Int. Symp. on Degradation of Materials in Nuclear Power Systems - Water Reactors (1991)
9. S. E. Ziemniak and R. A. Castelli, J. Phys. Chem. Solids 64, 2081 (2003)
10. J. D. Dunitz and L. E. Orgel, J. Phys. Chem. Solids 3, 318 (1957)

TABLE I

Alloy 600 Corrosion and Release/Pickup Estimates Obtained by Gravimetric Analyses

| Exposure Time, hr | Weight Change During Test, mg | Base Metal Oxidized, mg | Zero Release[a] Wgt change, mg | % Release |
|---|---|---|---|---|
| 1000 | -0.39±0.25 | 0.19±0.04 | 0.03 | >100 |
| 2000 | -0.39±0.26 | 0.32±0.08 | 0.06 | >100 |
| 3000 | -0.27±0.32 | - | | |
| 5000 | -0.34±0.33 | 1.20±0.10 | 0.22 | 39% |
| 5000 | -0.54±0.10 | 1.49±0.17 | 0.27 | 46% |
| 8,000 | -0.26±0.44 | 1.04±0.18 | 0.19 | 37% |
| 10,000 | -0.54±0.28 | 1.65±0.21 | 0. 30 | 43% |

[a] 0.184 x column III

TABLE II

Indexed GIXRD Peaks for Corroded Alloy 600 Specimen (AX06, 10,000 hrs), ($\phi$ = 0.5º)

| Reflection Plane Indices, hkl | $2\theta_{obs}$ | $2\theta_{cor}$ | Reflection Plane Indices, hkl | $2\theta_{obs}$ | $2\theta_{cor}$ | Reflection Plane Indices, hkl | $2\theta_{obs}$ | $2\theta_{cor}$ |
|---|---|---|---|---|---|---|---|---|
| Spinel Phase | | | Nickel (Alloy) Phase | | | Recrystallized Nickel Phase | | |
| 220 | 22.425 | 22.364 | | | | | | |
| 311 | 26.351 | 26.291 | | | | | | |
| | | | 111 | 32.531 | 32.471 | 111 | 32.782 | 32.722 |
| | | | 200 | 37.663 | 37.603 | 200 | 38.081 | 38.021 |
| 440 | 45.776 | 45.717 | | | | | | |
| | | | 220 | 54.405 | 54.346 | 220 | 54.935 | 54.876 |
| | | | 311 | 64.800 | 64.741 | 311 | 65.438 | 65.379 |
| Lattice Parameter ($a_o$, D) | | 8.3767 (31) | Lattice Parameter ($a_o$, D) | | 3.5628(10) | Lattice Parameter ($a_o$, D) | | 3.5313(7) |

TABLE III

Surface oxide thicknesses of Alloy 600 based on intensity of O(1s) XPS peak and inferred substrate composition at large sputter depths (oxygen <5 at.%)

| Specimen ID (exposure time, hr) | O(1s) depth, D | Elemental distribution, wgt.% Ni | Cr | Fe |
|---|---|---|---|---|
| I84 (1000) | 185 | 77.2 | 16.8 | 6.1 |
| I82 (2000) | 175 | 78.7 | 16.6 | 4.7 |
| I74 (5000) | 175 | 77.0 | 17.3 | 5.7 |
| I96 (5000) | 219 | 76.7 | 17.5 | 5.8 |
| I90 (8000) | 222 | 71.4 | 18.3 | 7.3 |
| I70 (10,000) | 260 | 74.7 | 18.4 | 6.9 |
| | Avg: | 76.4±1.5 | 17.5±0.7 | 6.1±0.8 |
| | Assay of Alloy 600: | 74.0 | 16.1 | 9.0 |

TABLE IV

NiCrFe Alloy 600 Corrosion Film Characterization
by Integration of Speciated XPS Composition vs. Depth Profile

| Exposure Time, hrs. | Metal Ion Content, mg $dm^{-2}$ | Distribution, wgt% | | | | Recrys. Ni, mg $dm^{-2}$ |
|---|---|---|---|---|---|---|
| | | Ni(II) | Cr(III) | Fe(II,III) | Zn(II) | |
| 1000 (I84) | 0.78 | 21.8 | 47.4 | 15.4 | 15.4 | 0.25 |
| 2000 (I82) | 0.77 | 11.7 | 50.6 | 18.2 | 19.5 | 0.38 |
| 5000 (I74) | 0.71 | 8.5 | 50.7 | 21.1 | 19.7 | 0.58 |
| 5000 (I96) | 1.15 | 8.7 | 52.2 | 21.7 | 17.4 | 0.72 |
| 8000 (I90) | 1.17 | 6.0 | 52.1 | 23.9 | 17.9 | 0.98 |
| 10,000 (I70) | 1.36 | 5.9 | 54.4 | 19.8 | 19.8 | 1.05 |
| | Avg. | 10.4 | 51.2 | 20.0 | 18.3 | |

Table V

Material balances for chromium, iron and nickel during corrosion of NiCrFe Alloy 600 in zinc-treated water

| | Cr(III), mg $dm^{-2}$ | | Fe(II,III), mg $dm^{-2}$ | | Ni(II),mg $dm^{-2}$ | | | | |
|---|---|---|---|---|---|---|---|---|---|
| Exposure Time, hr | Corroded * per Table I | Found in Scale (Table IV) | Corroded * per Table I | Found in Scale (Table IV) | Corroded* per Table I | Found in Scale (Table IV) | Recrys. Ni(0) (Table IV) | Loss** | Corrosion Release, % |
| 1000 | 0.17 | 0.37 | 0.09 | 0.12 | 0.77 | 0.17 | 0.25 | 0.35 | 45 |
| 2000 | 0.24 | 0.39 | 0.13 | 0.14 | 1.09 | 0.09 | 0.38 | 0.62 | 57 |
| 5000 | 0.37 | 0.36 | 0.21 | 0.15 | 1.73 | 0.06 | 0.58 | 1.09 | 63 |
| 5000 | 0.37 | 0.60 | 0.21 | 0.25 | 1.73 | 0.10 | 0.72 | 0.91 | 53 |
| 8000 | 0.48 | 0.61 | 0.27 | 0.28 | 2.18 | 0.07 | 0.98 | 1.13 | 52 |
| 10,000 | 0.53 | 0.74 | 0.30 | 0.27 | 2.44 | 0.08 | 1.05 | 1.31 | 54 |
| | | | | | | | | | avg. 54±5 |

* Non-selective oxidation hypothesis applied to parabolic correlation: $0.033\ t^{1/2}$.

** Closure of balance for nickel is demonstrated by allowing for loss, i.e., release to aqueous phase.

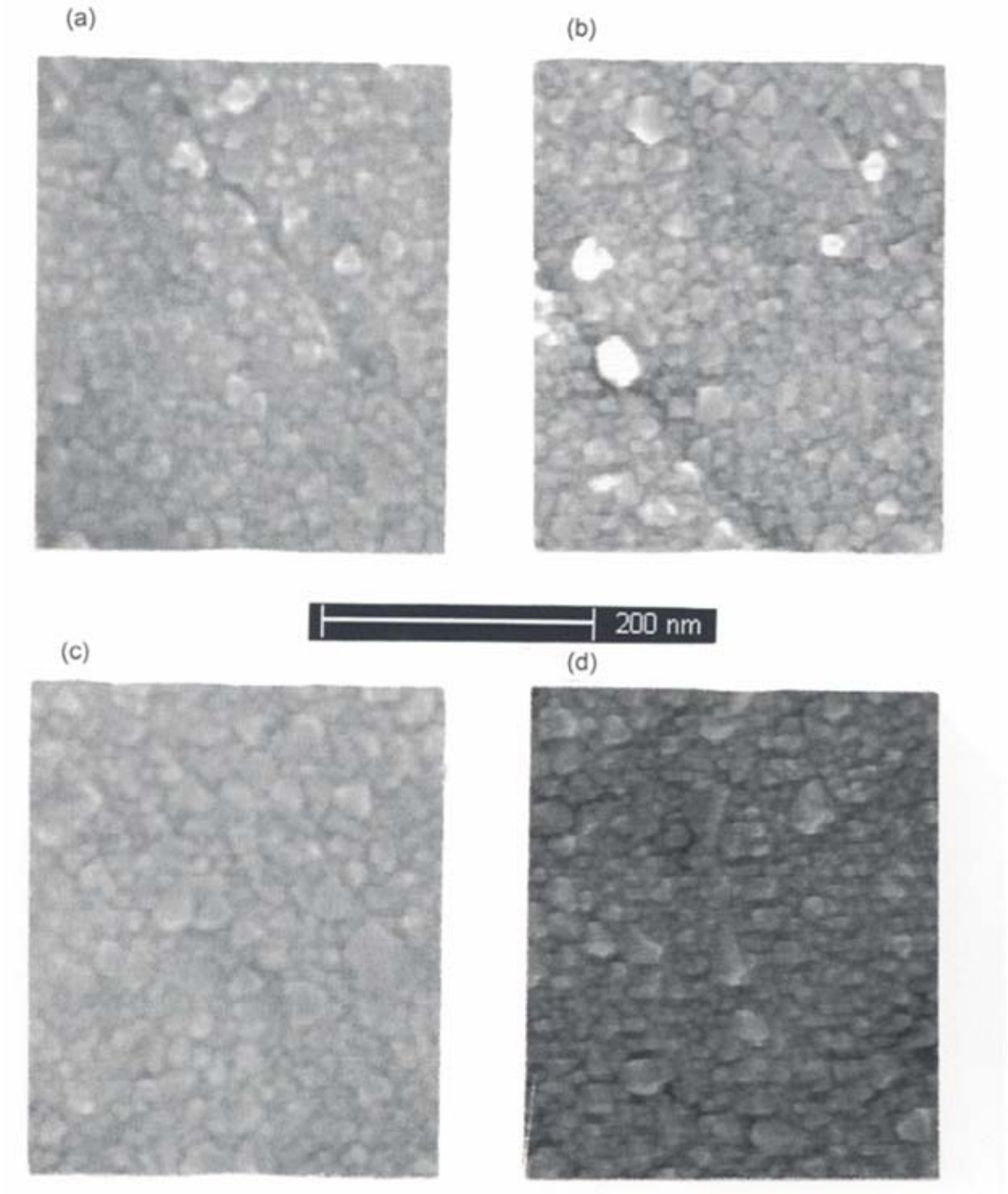


Fig. 1. High magnification SEM photographs of Alloy 600 after exposure to zinc-treated, hydrogenated water at 260°C: (a) 1000 hr, (b) 2000 hr, (c) 5000 hr, (d) 10,000 hr.

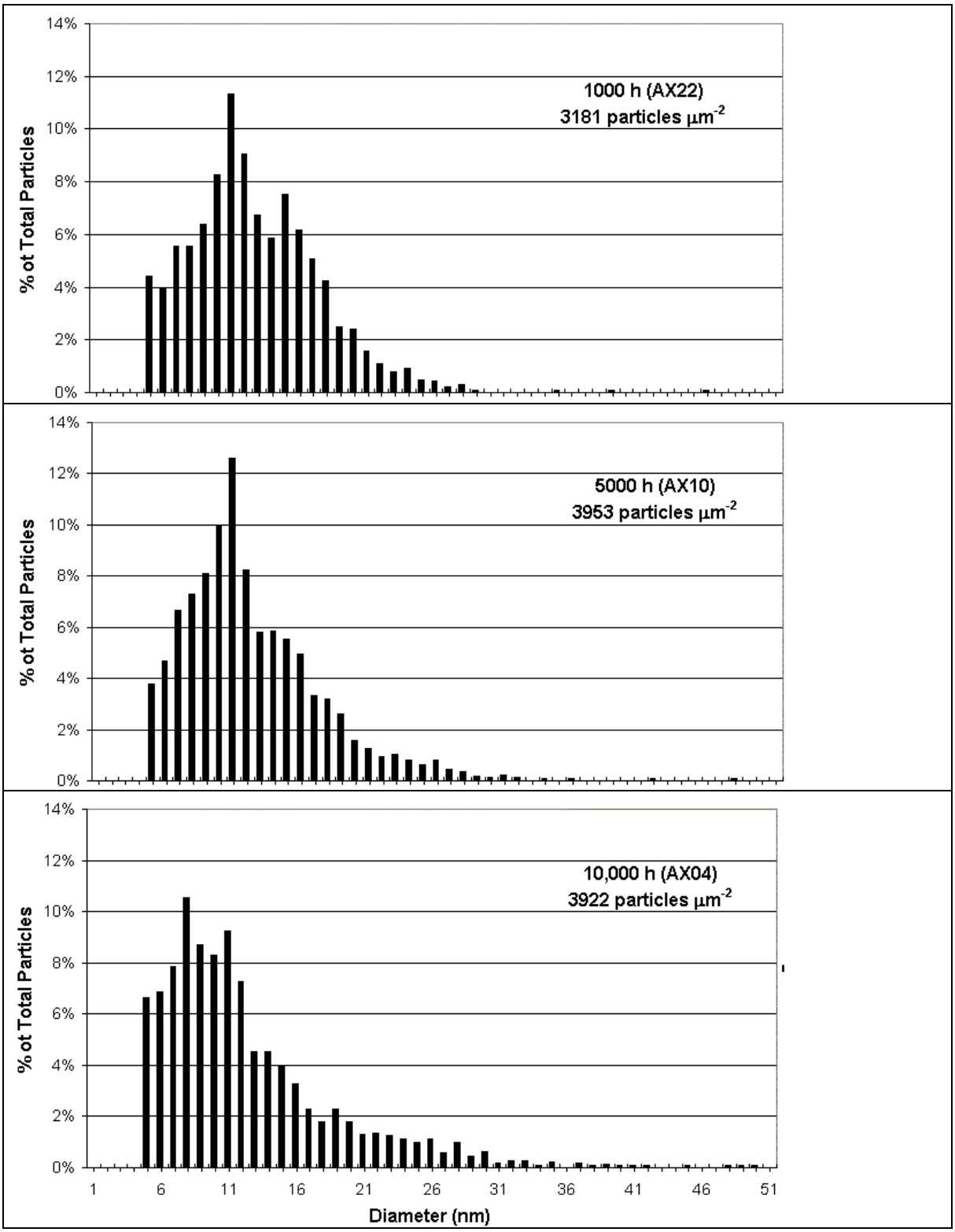


Fig. 2. Size distributions of corrosion oxide crystals observed by FEG-SEM in Fig. 1.

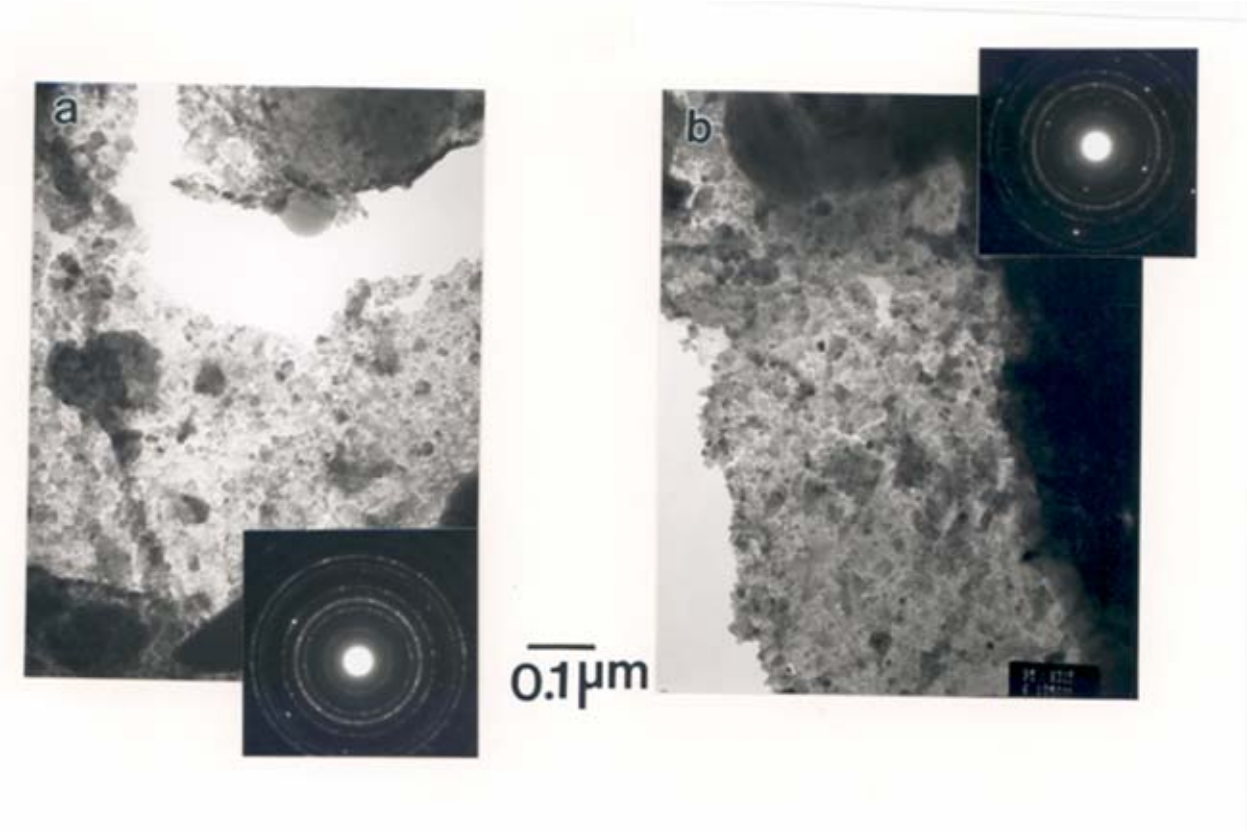


Fig. 3. Bright field TEM photographs taken through Alloy 600 corrosion layer on 10,000 hr specimen (I68), including electron diffraction pattern.

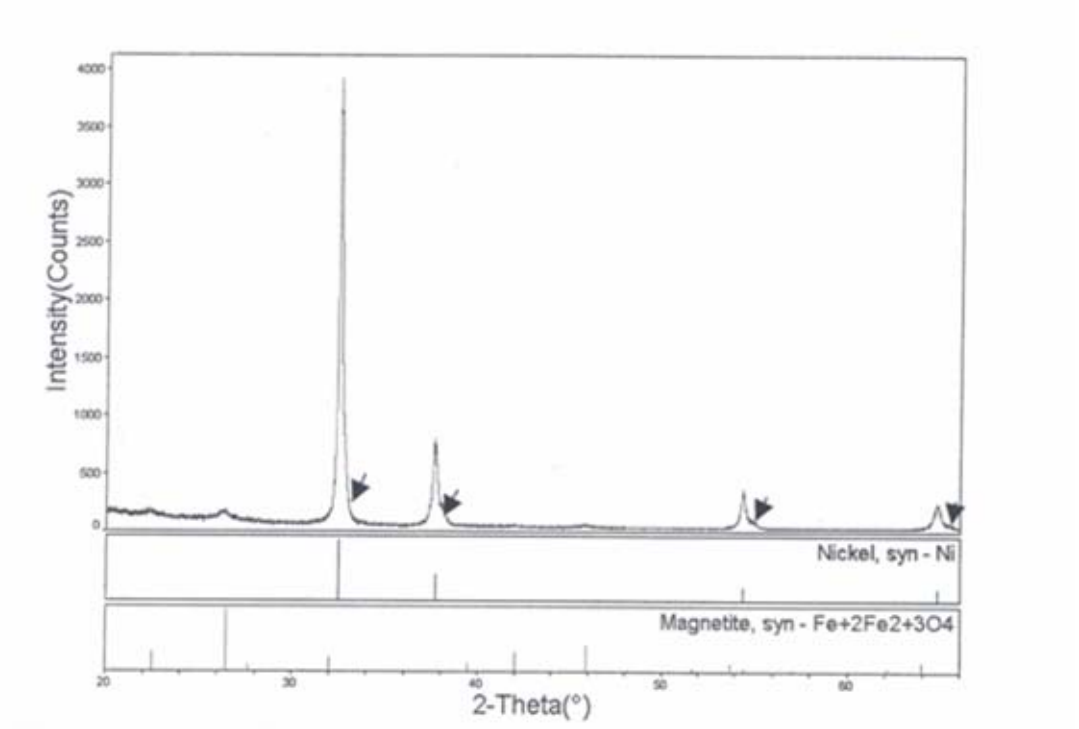


Fig. 4. Grazing incidence XRD pattern for 10,000 hr corrosion specimen (AX06) at $\phi$ = 0.5º. Arrows indicate presence of shoulder peaks attributed to recrystallized nickel.

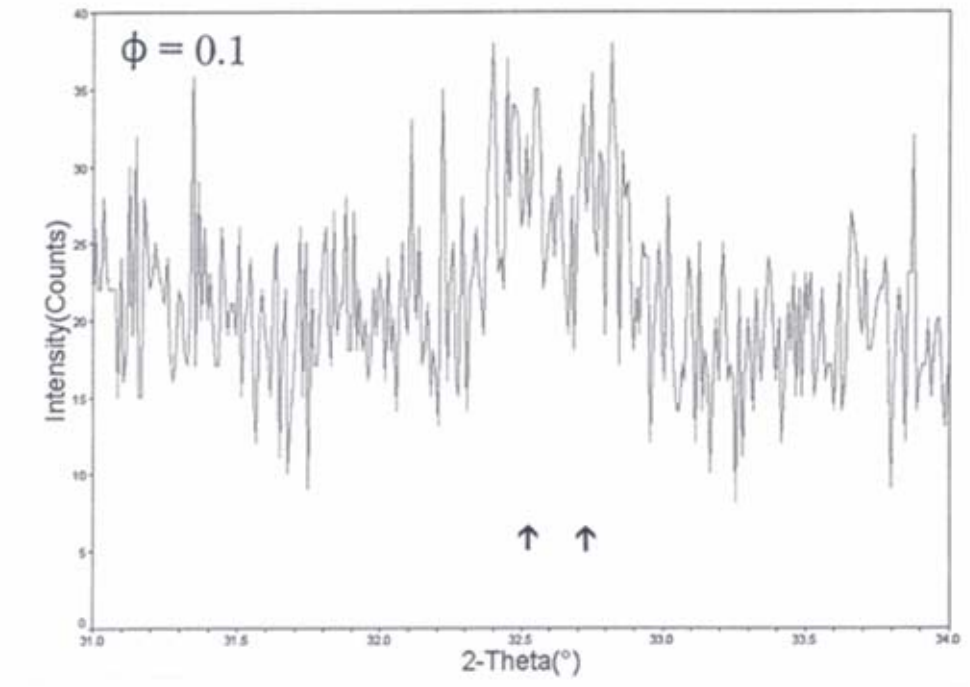


Fig. 5. Expanded 2**2** region of GIXRD pattern collected for 10,000 hr corrosion specimen in vicinity of Alloy 600 nickel [111] peak at **N** = 0.1°. Arrows denote peak positions for Alloy 600 and recrystallized nickel.

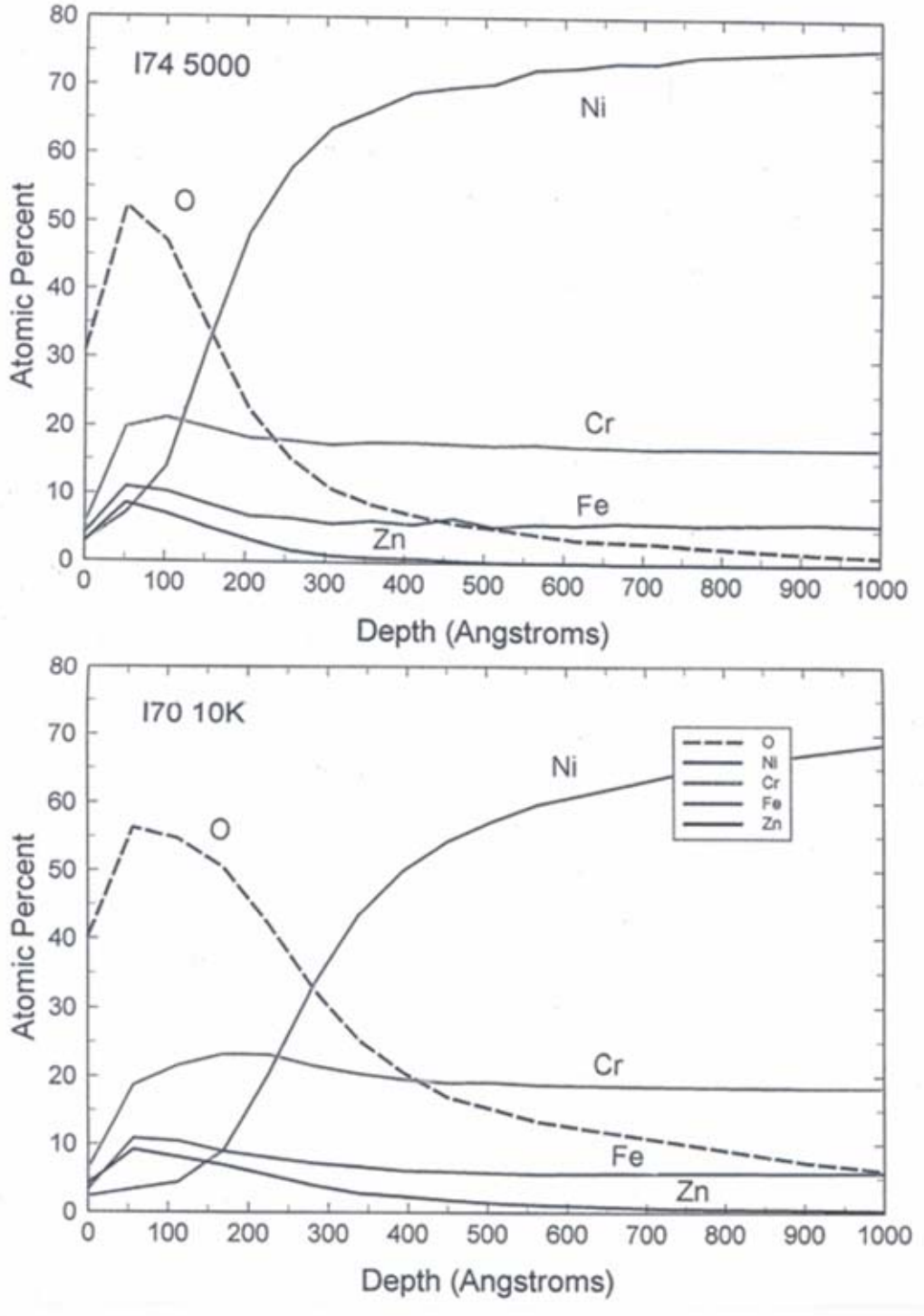


Fig. 6 Elemental composition versus depth profiles on Alloy 600 surfaces exposed to hydrogenated, zinc-treated water at 260°C for: (a) 5000 hr and (b) 10,000 hr.

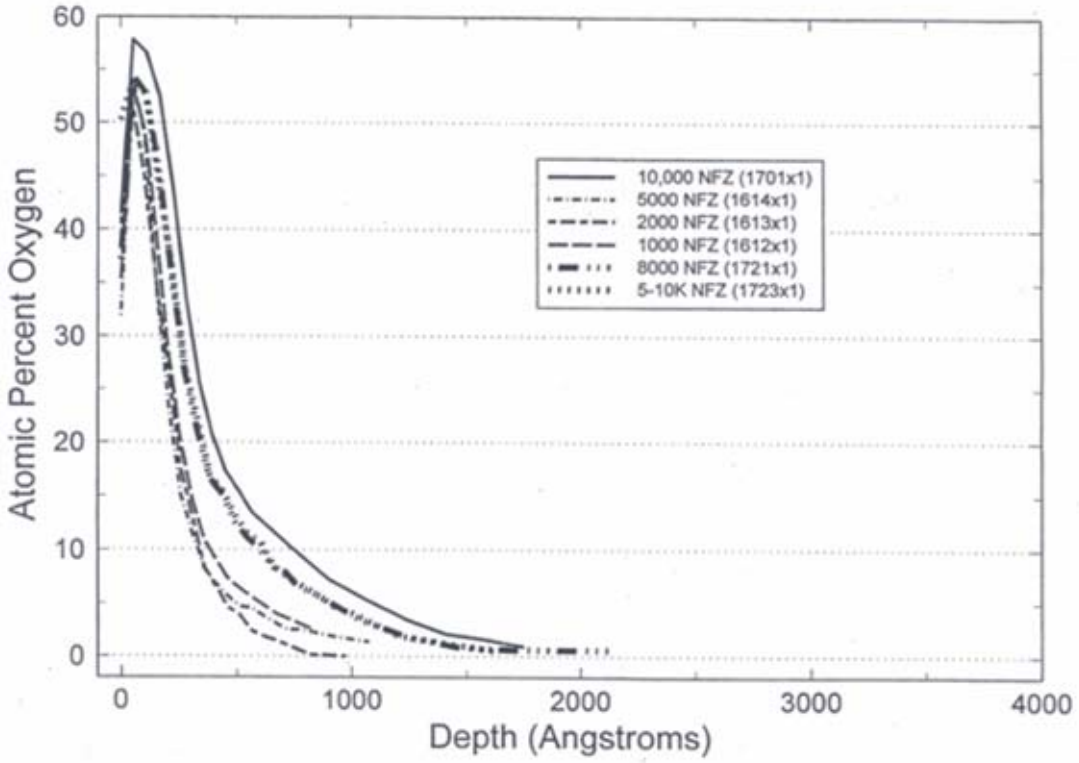


Fig. 7. Superimposed oxygen versus depth profiles on corroded Alloy 600 surfaces for exposure times between 1000 and 10,000 hrs.

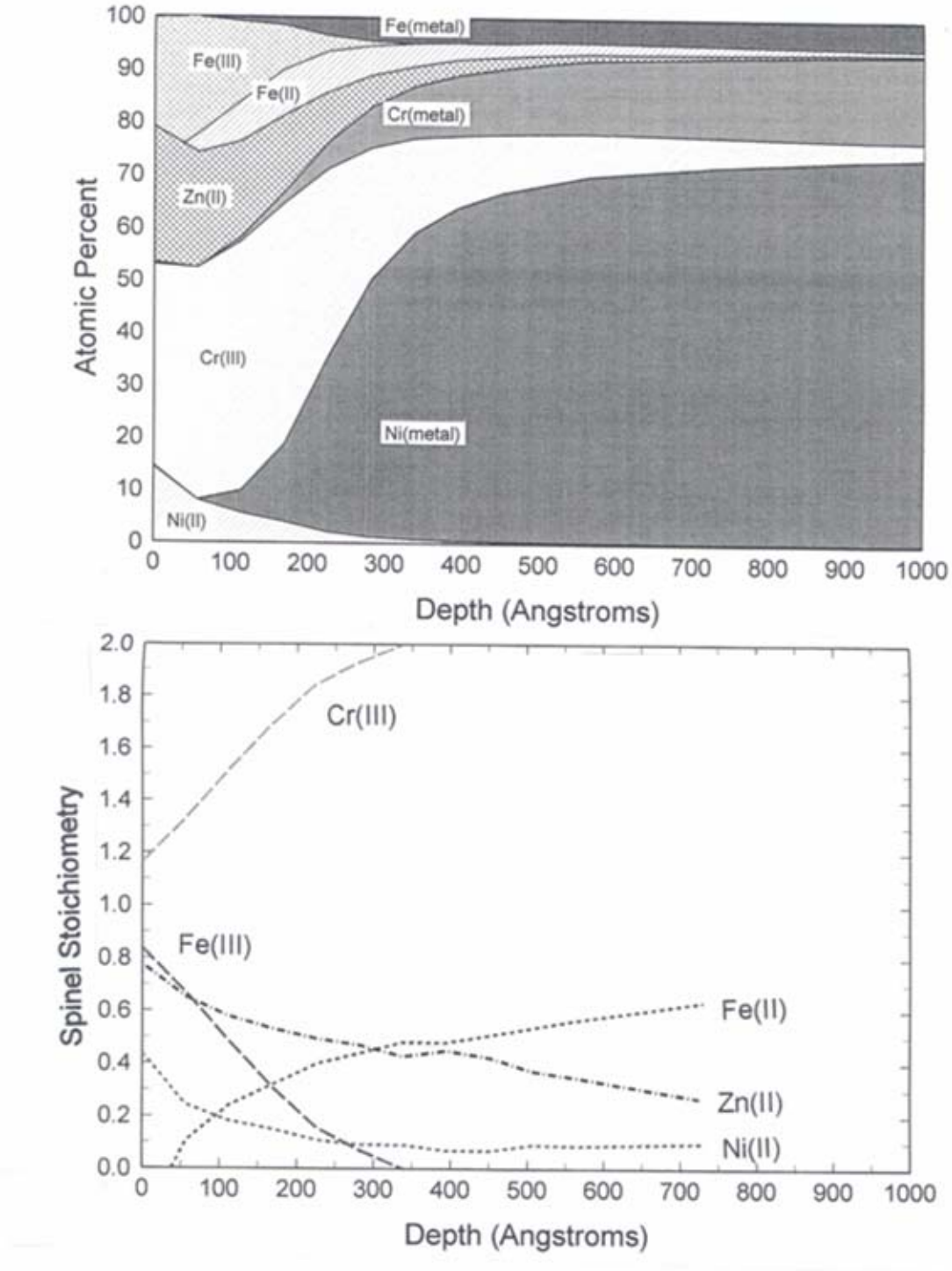


Fig. 8. Speciated composition versus depth profile on Alloy 600 specimen exposed to hydrogenated, zinc-treated water at 260°C for 10,000 hr (I70): (a) oxidized/unoxidized metal splits (cross-hatched/solid) and (b) indicated stoichiometry of spinel oxide.

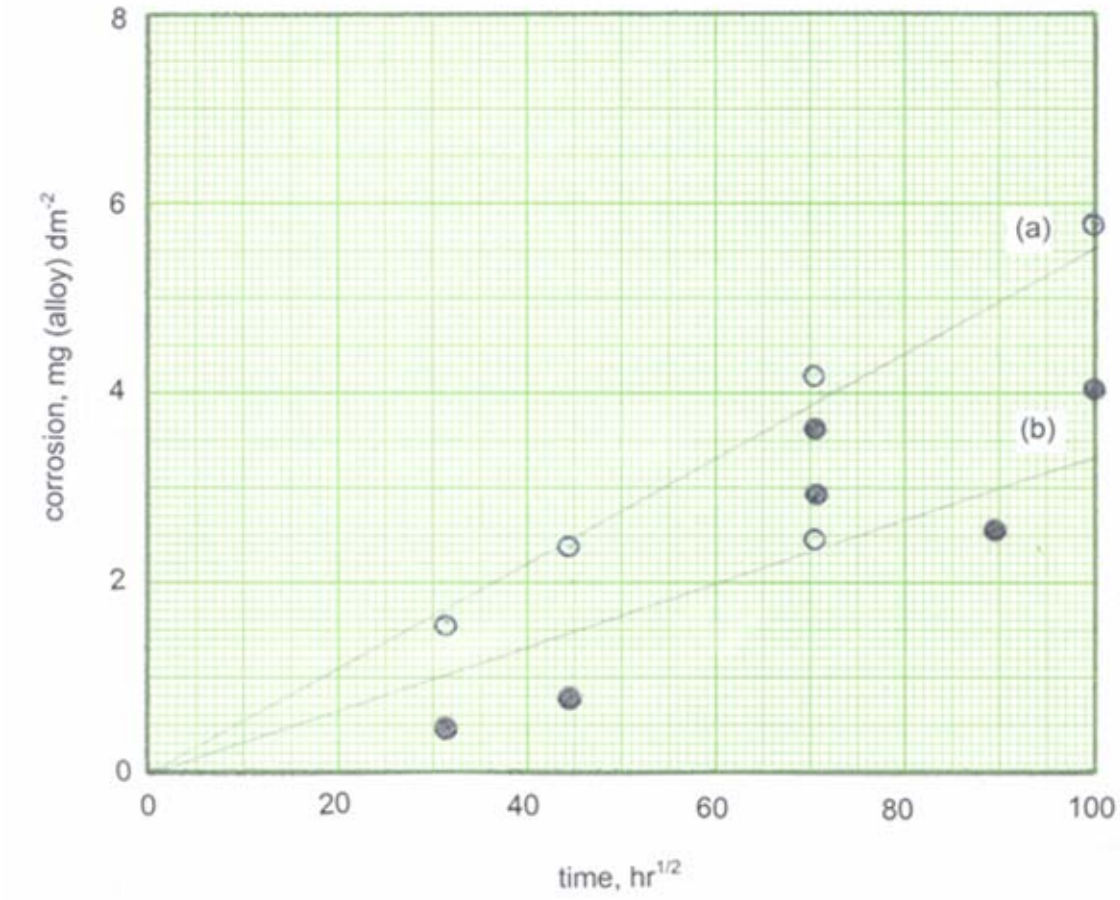


Fig. 9. Effect of zinc treatment on corrosion rate of Alloy 600 in hydrogenated water at 260°C: (a) non-zinc baseline [2] and (b) 30 ppb Zn(II) added.